Insight into the Strategies for Improving Thermal Stability of Efficient N-Type Mg_3Sb_2-Based Thermoelectric Materials

Jiawei Zhang,* Lasse Rabøl Jørgensen, Lirong Song, and Bo B. Iversen*

Center for Integrated Materials Research, Department of Chemistry and iNANO, Aarhus University, DK-8000 Aarhus, Denmark.

KEYWORDS: *thermoelectric, thermal stability, kinetic effect, n-type $Mg_3(Sb,Bi)_2$, Mg vapor annealing, X-ray and neutron diffraction*

ABSTRACT: n-type $Mg_3(Sb,Bi)_2$ compounds recently have been demonstrated as promising low-cost efficient thermoelectric materials in low and intermediate temperature ranges; however, thermal stability of this type of material still poses a great challenge for practical applications. In this work, we conduct a systematic investigation of thermal stability of several high-performing n-type $Mg_3(Sb,Bi)_2$-based thermoelectric materials in both bulk and powdered forms using X-ray and neutron diffraction. It is found that the bulk sample exhibits a much slower degradation rate based on the evolution of the secondary Bi/Sb phase in comparison with the powdered sample, revealing a clear kinetic effect. Moreover, the surface of the bulk sample will gradually become Mg poor or Bi rich even at room temperature when exposed to air for a long time, highlighting the importance of surface encapsulation for applications. An underlying mechanism based on the Mg loss/migration is proposed to account for the property degradation. Importantly, to address the property degradation we discuss possible solutions and propose Mg-vapor annealing as an effective approach to enhance thermal stability by suppressing the Mg loss/migration through saturating grains and grain boundaries with elemental Mg. We expect a combination of the Mg-vapor annealing and surface coating to further improve the long-term thermal stability. This work sheds light on the strategies for enhancing the long-term stability of n-type Mg_3Sb_2-based thermoelectrics for practical applications.

1. INTRODUCTION

Thermoelectric (TE) materials can directly convert heat into electrical energy, which offers a green and sustainable solution for waste heat harvesting.[1-3] The efficiency of a TE material is typically characterized by the so-called figure of merit, $zT = \alpha^2\sigma T/\kappa$, where α, σ, κ, and T denote the Seebeck coefficient, electrical conductivity, thermal conductivity, and absolute temperature, respectively. Developing low-cost efficient TE materials with good thermal stability is imperative for their widespread applications. Recently, the success of n-type doping with tellurium has stimulated the discovery of novel high-performance n-type $Mg_3(Sb,Bi)_2$ materials with low cost and earth-abundant elements.[4-6] There are a variety of studies reporting superior zT values of n-type $Mg_3(Sb,Bi)_2$ materials at low and intermediate temperatures,[5-14] whereas systematic thermal stability investigations of these compounds are very limited. Thermal stability, however, is as important as high zT values when considering the practical applications of TE materials.

Thermal stability issues regarding n-type $Mg_3Sb_{1.475}Bi_{0.475}Te_{0.05}$ were first reported in 2018 by Jørgensen et al.,[15] where powdered samples were exposed to temperatures up to 725 K in air for ten thermal cycles while being characterized with powder X-ray diffraction (PXRD) and pair distribution function (PDF) techniques. Up to 11 wt% of crystalline bismuth phase was observed already after the first heating cycle, which gradually increased to about 15 wt% during the ten thermal cycles. From a decrease in the unit cell parameter and PDF analysis before and after heating, it was concluded that bismuth was thermally released from the crystal structure of the $Mg_3(Sb,Bi)_2$-phase. The study was originally motivated by a hysteresis behavior of the electrical properties (resistivity and Seebeck coefficient) during multiple thermal cycles, which include a clear difference between the first thermal cycle and subsequent ones, observed by both Zhang *et al*.[5] and Tamaki *et al*.[6] However, whether the release of bismuth from the structure is responsible for the temperature dependency of the physical properties could not be concluded, as physical property measurements are performed on densely compacted bulk samples rather than fine powders. The stability of bulk samples of n-type $Mg_3Sb_{1.5}Bi_{0.5}$ derivatives has been investigated further from the time dependency of the Hall carrier concentration.[16-18] For a Te-doped $Mg_3Sb_{1.5}Bi_{0.5}$ bulk sample, the carrier concentration was observed by Imasato *et al.*[16] to decrease from approximately 3×10^{19} cm^{-3} to 1.5×10^{19} cm^{-3} within hours at 723 K in a dynamic vacuum. Cation-site doping with heavier elements such as La,[16] Y,[17] and Yb[18] seems to improve high-temperature stability with a clear suppression of carrier concentration degradation. In addition, surface coating with BN has been shown to enhance the high-temperature stability of n-type $Mg_3(Sb,Bi)_2$ derivatives.[19] The property degradation was suggested to be related to the evaporation of electron-donating Mg atoms from the sample due to the high vacuum and high-temperature environment during Hall carrier concentration measurements; however, the underlying degradation mechanism remains largely unclear. Thus, a detailed analysis of diffraction data on bulk samples and degradation

mechanisms is desirable for enhancing thermal stability of n-type $Mg_3(Sb,Bi)_2$.

In this work, we start with a detailed investigation of thermal stability of bulk and powdered n-type Te-doped $Mg_3Sb_{1.5}Bi_{0.5}$ using multi-temperature X-ray and neutron scattering techniques. We reveal a clear kinetic effect with bulk samples showing a much slower degradation than powders owing to a much smaller exposed surface area to volume ratio. This effect is also consistently observed in Se-doped and S-doped $Mg_3Sb_{1.5}Bi_{0.5}$ samples, indicative of a general feature of the $Mg_3(Sb,Bi)_2$ system. In addition, we found that the surfaces of bulk samples gradually become Bi rich when exposed to ambient conditions for a long time (≥ 1 year). To understand the degradation, we propose a three-step degradation mechanism based on Mg migration/loss, where the key step for degradation is the Mg loss of the $Mg_3(Sb,Bi)_2$ grains. We propose that Mg-vapor annealing is an effective approach for improving thermal stability as it can saturate the grains and grain boundaries with elemental Mg, which serves as an energy barrier for suppressing the Mg migration/loss. Finally, we discuss other potential solutions, and propose the combination of the Mg-vapor annealing and surface coating as a possible future direction for further improvement of the long-term stability of n-type $Mg_3(Sb,Bi)_2$ TEs.

2. EXPERIMENTAL SECTION

2.1 Sample synthesis and structural characterization

n-type $Mg_3Sb_{1.475}Bi_{0.475}Te_{0.05}$, $Mg_3Sb_{1.5}Bi_{0.48}Se_{0.02}$, and $Mg_3Sb_{1.5}Bi_{0.49}S_{0.01}$ samples, as well as a $Mg_3Sb_{1.5}Bi_{0.5}$ sample, were synthesized from high-purity raw elements of Mg powders (99.8%, ≤44 μm, Alfa Aesar), Sb pieces (99.9999%, ChemPUR), Bi pieces (99.999%, ChemPUR), Te pieces (99.999%, Sigma Aldrich), Se shots (>99.999%, Alfa Aesar), and S powders (99.9%, Sigma-Aldrich) using arc melting followed by the spark plasma sintering (SPS) pressing. The synthesis details have been described in references [5,20,21]. The n-type $Mg_{3.5}Sc_{0.04}Sb_{1.97}Te_{0.03}$ sample, as well as the Mg_3Sb_2 sample, were prepared from a mixture of Mg powder (99.8%, -325 mesh, Alfa Aesar), Sb powder (99.5%, -325 mesh, ChemPUR), Te powder (99.99%, -325 mesh, Alfa Aesar) and Sc powder (99.9%, -100 mesh, ChemPUR) using the direct spark plasma sintering method, which has been described in detail in reference [22]. The Mg-vapor annealing experiment was conducted using the setup shown in Figure S1 similar to the method proposed by Wood *et al.*[23] The as-pressed pellets in direct contact with Mg turnings (99.5%, ChemPUR) were placed in a glassy carbon crucible and annealed in Ar flow.

The structural evolution of the bulk samples after each step of post-treatment was tracked by PXRD measurements using Bragg-Brentano geometry and a Cu Kα_1 source on a Rigaku Smartlab X-ray diffractometer. Analysis of the microstructure and elemental distribution of $Mg_{3.5}Sc_{0.04}Sb_{1.97}$ $Te_{0.03}$ and $Mg_3Sb_{1.475}Bi_{0.475}Te_{0.05}$ was conducted on a FEI Nova NanoSEM 600 scanning electron microscope (SEM) with an energy dispersive spectrometer (EDS).

2.2 Multi-temperature in-house PXRD

Multi-temperature in-house PXRD data were collected on a Rigaku Smartlab diffractometer in reflection geometry with a Co-source and a monochromator to provide Co-K_α radiation with wavelengths of 1.78892 Å and 1.79278 Å. Here, the bulk and powder samples were thermally cycled between 300 K and 725 K for two and three cycles, respectively, in an Anton Paar DHS 1100 domed heating stage with a dynamic vacuum atmosphere. The heating/cooling rate was 2 K min^{-1}.

2.3 Multi-temperature synchrotron PXRD

Synchrotron PXRD experiments performed on powdered samples were conducted at SPring-8 in Japan, at beamline BL44B2 with an X-ray wavelength of 0.5 Å.[24] Diffraction data were collected at temperatures between 300 K and 725 K in steps of 100 K for two thermal cycles. The exposure time at each temperature was 7 minutes, which was followed by a 1-2 minute equilibration time at each temperature. The powdered sample was floated three times in ethanol to filter out large particles. The remaining fine powder was then packed in a quartz capillary with a 0.2 mm inner diameter with an Ar atmosphere. No data refinement was carried out on these datasets. In addition, synchrotron PXRD experiments of several powdered samples were conducted for ten thermal cycles at 300-725 K using a photon energy of 100 keV at the beamline P21.1, PETRA, DESY, Germany.

2.4 Neutron time-of-flight diffraction

Neutron time-of-flight (TOF) diffraction data were collected at the ISIS Neutron and Muon Source in the UK, at the Polaris beamline.[25] Here, a dense pellet was placed in a vanadium can with 11 mm diameter and thermally cycled between 300 K and 725 K in a dynamic vacuum atmosphere. Data were likewise collected in steps of 100 K with a heating rate of 2 K min^{-1}. At each temperature, the temperature was allowed to stabilize for 10 minutes, and the data were then acquired for 40 minutes.

2.5 Rietveld refinements

Rietveld refinements of the in-house PXRD data collected on the bulk sample were carried out using the FullProf Suite.[26] The Mg_3Sb_2 structure (ICSD #2142) was used as a starting model for the $Mg_3Sb_{1.475}Bi_{0.475}Te_{0.05}$ phase without including Bi and Te in the refinement model. Here, the unit cell parameters and scale factor were refined, which yielded a good initial description of the data. Afterward, manually selected and linearly splined background points were introduced to the model, together with the isotropic atomic displacement parameters of all atoms in the unit cell. The peak shapes were described using the Thompson-Cox-Hastings pseudo-Voigt profile function,[27] where the angular independent broadening term, *W*, and the Lorentzian strain parameter, *X*, were refined. The results of the refinements are shown in Table S1.

For powder neutron TOF diffraction data refinements were carried out in Jana2006.[28] Here, banks 1-5 were included in the refinement. The peak profiles were described using a pseudo-Voigt function, where the Lorentzian linear broadening term, gam-1, was refined. The background was described using the Legendre polynomial function with 4 coefficients refined. The instrumental parameter called DIFC was refined, which relates the theoretical time-of-flight to its d-spacing. Once again, all isotropic atomic displacement parameters were refined. An example of refinement for all five banks can be seen in Figure S2, and details of the refinement results are shown in Table S2.

2.6 TE transport property measurements

High-temperature Hall and resistivity data of pellets were measured under dynamic vacuum on a home-built setup using a magnetic field of 1.25 T and the van der Pauw method.[29,30] High-temperature Seebeck coefficients were measured in a dynamic vacuum on an in-house system similar to the one

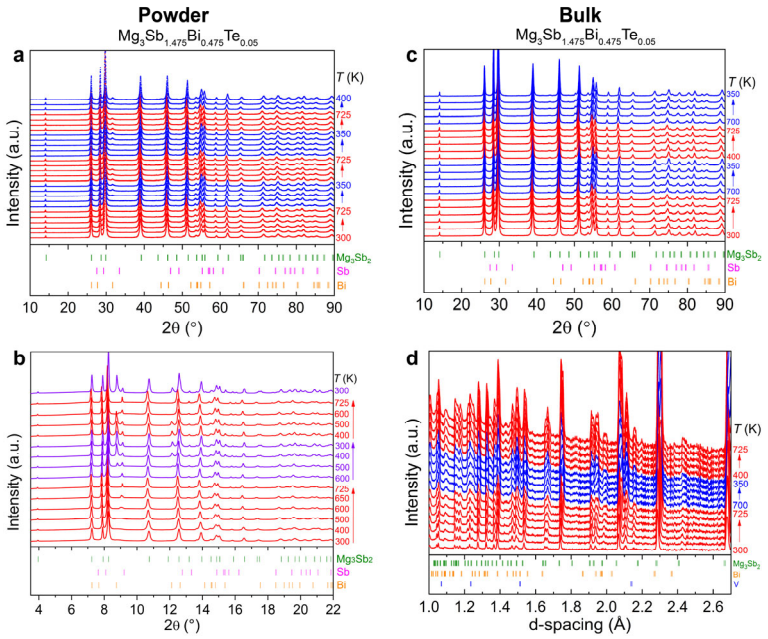

Figure 1. (a,b) Multi-temperature PXRD patterns from powdered $Mg_3Sb_{1.475}Bi_{0.475}Te_{0.05}$ samples obtained in-house (a) and using a synchrotron radiation (b). (c,d) Multi-temperature PXRD data from bulk $Mg_3Sb_{1.475}Bi_{0.475}Te_{0.05}$ samples obtained in-house (c) and using neutron TOF (d).

reported by Iwanaga *et al.*[31] Thermal conductivity was determined by $\kappa = dDC_P$, where the density (d) was estimated from the sample mass and volume, the thermal diffusivity (D) was measured using the laser flash method (Netzsch, LFA457), and the heat capacity (C_P) was indirectly derived using a Pyroceram 9606 standard sample in the LFA457 setup.

3. RESULTS AND DISCUSSION

3.1 Thermal stability: bulk *versus* powder

In this section, we first revisit the thermal stability of the Te-doped $Mg_3Sb_{1.5}Bi_{0.5}$ powders studied by combining multi-temperature synchrotron and in-house PXRD data. It is worth noting that the multi-temperature synchrotron PXRD data analyzed here were collected during another beam time at SPring-8, and thus different from those previously reported by Jørgensen *et al.*[15] For all PXRD data collections, fresh samples without a thermal history were used. The in-house and synchrotron multi-temperature PXRD data from powder samples are displayed in Figure 1a,b. It is found that Bi appears as a secondary phase at 500 K during the cooling segment of the first thermal cycle. This can be understood as the crystallization of Bi, which was expelled from the structure and has a melting point of ~544 K. When the temperature is higher than 544 K, Bi will melt, and the crystalline peak will disappear. In addition, as revealed by the synchrotron PXRD data a small amount of the secondary phase Sb appears as the temperature increases above 500 K in the first heating segment. The PXRD patterns of the first heating segment are different from those of the first cooling segment and the following thermal cycles, which fits well with the different behavior during the first heating segment of the electrical properties. After the first cycle, the PXRD data exhibits the same behavior upon repeated heating cycles, consistent with electrical properties remaining unchanged between thermal cycles. High-resolution synchrotron PXRD captures the subtle structural evolutions of the minor secondary phases of Bi and Sb as a function of the temperature. The multi-temperature synchrotron PXRD results presented here are in good agreement with what was reported by Jørgensen *et al.*[15]

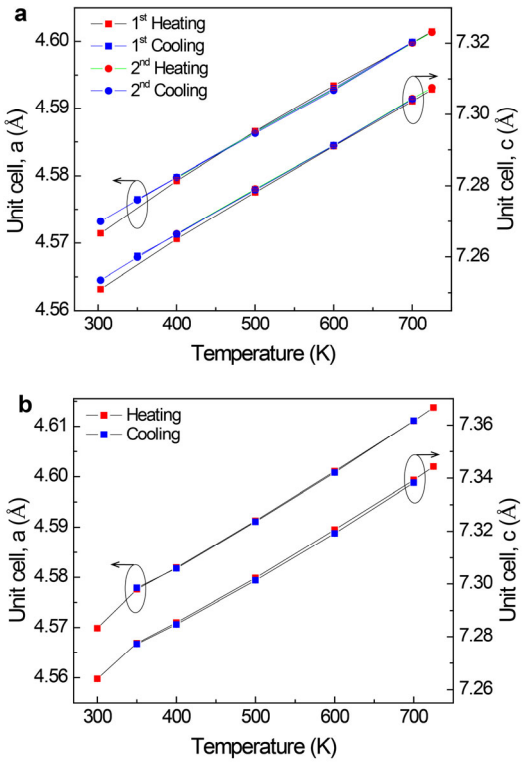

Figure 2. Temperature dependence of the lattice parameters, a and c, extracted from the Rietveld refinements of the multi-temperature diffraction data from $Mg_3Sb_{1.475}Bi_{0.475}Te_{0.05}$ bulk samples, recorded in-house (a) or using neutron TOF (b).

We next turn to investigate the thermal stability of bulk samples using X-ray and neutron scattering. A densified pellet of nominal composition $Mg_3Sb_{1.475}Bi_{0.475}Te_{0.05}$ was exposed to

two heating cycles from 300 to 725 K, while diffraction data were recorded using an in-house diffractometer. The diffraction data are shown in Figure 1c. Here, it is expected that a secondary bismuth phase would appear when cooling the sample after the first heating cycle, but interestingly, there is no sign of a secondary bismuth phase in the bulk sample even after two thermal cycles. In the study by Jørgensen *et al.,*[15] it was shown that the unit cell size of the Mg_3Sb_2-phase is significantly influenced by the release of bismuth. In Figure 2a, the unit cell parameters extracted from Rietveld refinements are shown to quantitatively monitor the behavior of the Mg_3Sb_2-phase during the heating cycles (see also Table S1). Here, no apparent difference is observed between the first and subsequent heating cycles, indicating a higher stability of the $Mg_3Sb_{1.5}Bi_{0.5}$-phase in bulk compared with fine powders. The diffraction data shown in Figure 1c were collected using a parallel beam in reflection geometry and a Co-K_α X-ray source, and the penetration depth of the relatively low-energy X-rays will be very limited due to the presence of heavy elements such as bismuth and antimony. The observed diffraction mainly originates from the surface of the sample.

To investigate the interior of the bulk sample, neutron TOF diffraction data were measured during two thermal cycles, and the data can be seen in Figure 1d. Neutrons interact weakly with solid matter compared to X-rays, and thick samples can therefore be measured in transmission geometry without significant absorption issues. The weak interaction, however, comes with the downside of a lower signal-to-noise ratio compared to X-rays, despite having a longer exposure time. During the two thermal cycles, the diffraction peaks from the Mg_3Sb_2-phase become sharper, which is particularly evident for the peaks at about 1.7 Å and just below 1.5 Å. This is presumably due to the thermal release of residual microstructural strain from the synthesis. This is further supported by the stagnation of the evolution during cooling, and continuation during the second heating. Just below 2.2 Å, a new peak seems to appear, which can be indexed to the vanadium sample holder. Furthermore, there is no clear diffraction peak from elemental bismuth detected during the experiment. Once again, the unit cell parameters for the Mg_3Sb_2-phase were extracted through structure refinement (see Figure S2 and Table S2) and are shown in Figure 2b. Similar to the PXRD experiment, we do not observe any difference in the unit cell size between the first and subsequent thermal cycles, indicating that no structural changes occur in the period of this experiment.

The difference in thermal stability between powders and bulks upon thermal cycling is a clear indication of a kinetic effect. It should be noted that this phenomenon is not limited to the $Mg_3Sb_{1.475}Bi_{0.475}Te_{0.05}$ sample. In Figure 3 we show the thermal stability of powdered and bulk n-type $Mg_3Sb_{1.5}Bi_{0.48}Se_{0.02}$ and $Mg_3Sb_{1.5}Bi_{0.49}S_{0.01}$ samples investigated by synchrotron and in-house multi-temperature PXRD (see also Figures S3 and S4), where a similar result is observed. The evolution of the secondary phases Bi/Sb is further confirmed in powdered samples of $Mg_3Sb_{1.5}Bi_{0.48}Se_{0.02}$ and $Mg_3Sb_{1.5}Bi_{0.49}S_{0.01}$ as well as $Mg_3Sb_{1.5}Bi_{0.5}$ and Mg_3Sb_2 by synchrotron multi-temperature PXRD data recorded over ten thermal cycles from 300 to 725 K (Figure S5), which were collected at the P21.1 beamline at DESY, Germany. One of the obvious differences between finely ground powders and densely compacted pellets is the surface-to-volume ratio, which is much higher for fine powdered samples than for pellets. In the literature, it has been suggested that Mg evaporation occurs during high-temperature measurements in a high vacuum.[16] No diffraction data were presented for the sample after stability tests, but it seems plausible that either Bi or Sb is expelled from the $Mg_3Sb_{1.5}Bi_{0.5}$ structure to rebalance the stoichiometry of the phase. Such an effect must be heavily dependent on the exposed surface area. In the powdered samples presented by Jørgensen *et al.*,[15] the crystallites were ground and floated before the experiment, which effectively separate small crystallites from larger ones. As such, these crystallites will have a large exposed surface area for the Mg evaporation/loss to occur, opposed to the bulk sample. Even so, long-term annealing experiments on bulk samples should still eventually reveal bismuth formation on the surface of the samples.

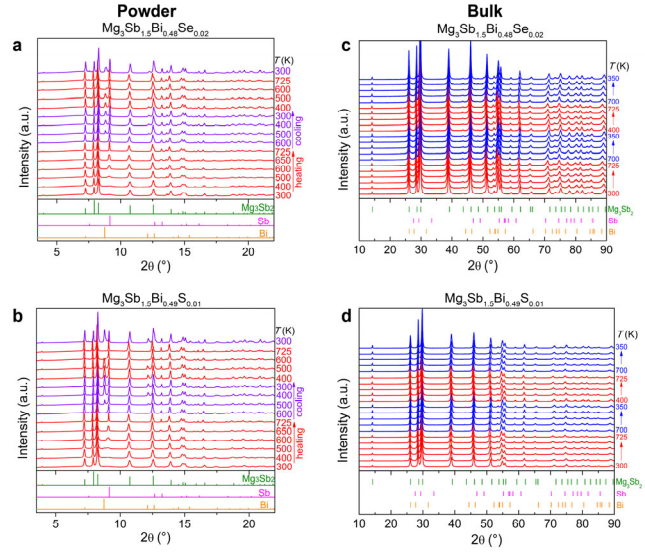

Figure 3. Multi-temperature PXRD patterns of samples with the compositions of (a, c) $Mg_3Sb_{1.5}Bi_{0.48}Se_{0.02}$ and (b, d) $Mg_3Sb_{1.5}Bi_{0.49}S_{0.01}$. The diffraction patterns were obtained from (a, b) powders at a synchrotron and from (c, d) bulk samples using a Rigaku Smartlab.

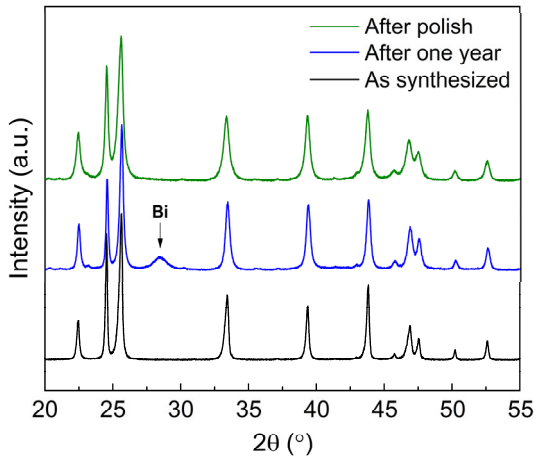

Figure 4. PXRD of the $Mg_3Sb_{1.475}Bi_{0.475}Te_{0.05}$ bulk sample after air exposure at room temperature for more than one year.

In Figure 4, PXRD data are presented for a pellet, which has been stored in air at room temperature for more than a year. Surprisingly, the long-term storage at ambient conditions has resulted in the elemental bismuth phase appearing on the surface of the sample. This observation can certainly not be

simply explained by evaporative loss of magnesium from the sample, as one does not expect magnesium to evaporate under ambient conditions. Instead, the formation of MgO on the surface is suggested as a mechanism that can resemble magnesium evaporation since we observed a change in sample surface after one-year exposure. This MgO on the sample surface usually appears in the amphous phase as it has not been through the heat treatment, and thus it is not detected by the PXRD. After polishing the pellet, the bismuth phase disappears completely, which further supports that bismuth is only formed on the sample surface. A similar surface effect has also been found in p-type Mg_3Sb_2 samples,[32] suggesting that it is a general effect in $Mg_3(Sb,Bi)_2$ compounds. In practical devices, surface coating or encapsulation should therefore be required to ensure stable applications.

3.2 Possible degradation mechanism

We next turn to discuss the possible degradation mechanism of $Mg_3(Sb,Bi)_2$. The dominant native defects in the $Mg_3(Sb,Bi)_2$ system are the negatively charged Mg vacancies,[33,34] which are the electron-capturing acceptors that prevent the Fermi level from moving towards the conduction bands. The defect formation energies of the negatively charged Mg vacancies are very sensitive to the local Mg concentration. As expected, when the $Mg_3(Sb,Bi)_2$ phase becomes Mg-poor, the negatively charged Mg vacancies form more readily due to lower formation energies, resulting in the reduction of electron concentration and n-type properties. The Mg loss from the bulk sample can be understood as two main effects. One is the loss at the sample surface, which can be attributed to evaporation/sublimation and/or the oxidation into MgO. The second is the loss within the sample, which can be attributed to migration/diffusion, which is reasonable considering the small, light nature of Mg atoms. Considering the mechanisms for the Mg loss above we can formulate a three-step degradation process based on the Mg loss (see Figure 5): (i) Mg leaves the $Mg_3(Sb,Bi)_2$ grains through migration/diffusion to the grain boundaries; (ii) then Mg migrates from the grain boundaries to the surface; (iii) Finally Mg is lost from the surface due to evaporation/sublimation or lost as MgO in air through oxidation.

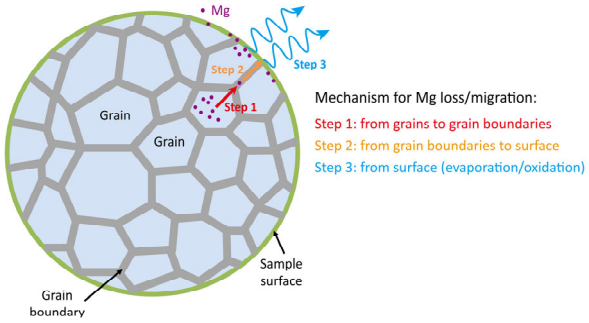

Figure 5. Schematic of the three-step degradation mechanism for the Mg loss/migration in $Mg_3(Sb,Bi)_2$.

Step (i) is the crucial step for property degradation, as the electron concentration should be closely related to the Mg loss from the $Mg_3(Sb,Bi)_2$ grains. The Mg loss from the structure, especially upon heat treatment, likely originates from the weaker bonding of Mg atoms in the octahedral sites.[35-37] The grain boundaries have been studied by the atom probe tomography, and are generally found to be Mg-deficient.[38] According to the classical diffusion/migration theory, the Mg atoms will tend to migrate/diffuse from high concentration regions (grains) to regions with a lower concentration (grain boundaries). Similarly, step (ii) can also be understood using the classical diffusion/migration theory, as the sample surface, which is exposed to the atmosphere, would continuously become Mg-poor over time. It should be noted that the grains on the sample surface exposed to the atmosphere will directly start the degradation from the step (iii), and thereby will show a much faster degradation than those of the sample interior, which explains the surface effect. The Mg loss through evaporation or oxidation in step (iii) is strongly dependent on the atmosphere (e.g. air, static/dynamic vacuum, static/dynamic inert gas, etc.) and temperature. A static atmosphere and a lower operational temperature would naturally result in enhanced stability as the Mg loss/migration rate is suppressed. As the Mg loss/deficiency of the system reaches a concentration limit, then Bi or Sb will be expelled into the grain boundaries from the $Mg_3(Sb,Bi)_2$ structure to rebalance the stoichiometry. The accumulation of the Bi or Sb secondary phases will result in significant inhomogeneity.[13] Especially, the Bi phase, with its very low melting point of ~544 K, will become a liquid at high temperatures, and thus be mobile within the grain boundaries. Furthermore, the molten Bi phase could even act as a flux and dissolve part of the grains or grain boundaries.

Note that step (i) is likely influenced by different synthesis methods resulting in different microstructures, grain sizes, and initial Mg content/distribution. Larger grains and a more homogeneous Mg distribution in as-synthesized samples are likely to result in improved thermal stability. It should be noted that the degradation mechanism discussed here simply provides a qualitative insight, which requires further detailed experimental investigation. The underlying mechanism might be more complicated than expected as it might involve a combination of multiple effects.

3.3 Strategies for improving long-term thermal stability

3.3.1 Mg-vapor annealing

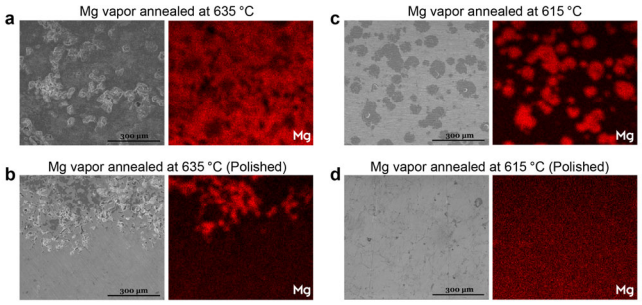

Figure 6. SEM and SEM-EDS images and elemental mappings of Mg on the surface of the $Mg_{3.5}Sc_{0.04}Sb_{1.97}Te_{0.03}$ pellet after the Mg-vapor annealing (a, b) at 635 ºC for 3 days unpolished (a) and polished (b) and (c, d) at 615 ºC for 3 days unpolished (c) and polished (d).

Considering Mg loss/migration as the main cause of the property degradation, then Mg-vapor annealing could be a straightforward approach to suppress the Mg loss/migration and improve thermal stability. Mg-vapor annealing provides a large magnesium reservoir that creates a Mg-rich environment, and saturates the gains and grain boundaries with elemental Mg in a relatively homogeneous manner. This ensures Mg-rich conditions for most grains and grain boundaries, which in

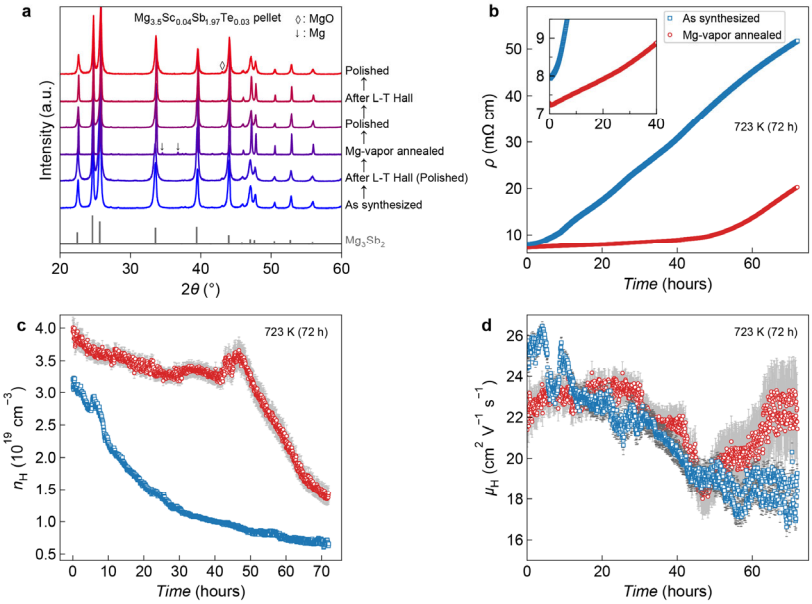

Figure 7. (a) PXRD patterns from the as-synthesized $Mg_{3.5}Sc_{0.04}Sb_{1.97}Te_{0.03}$ pellet before and after long-term (L-T) Hall measurements, as well as the Mg-vapor annealed $Mg_{3.5}Sc_{0.04}Sb_{1.97}Te_{0.03}$ pellet before and after long-term Hall measurements. (b) Electrical resistivity, (c) Hall carrier concentration, and (d) mobility as functions of the Hall measurement time for the Mg-vapor annealed $Mg_{3.5}Sc_{0.04}Sb_{1.97}Te_{0.03}$ sample compared with the as-synthesized sample.

principle will set an energy barrier that suppresses the Mg migration/loss from the grains and thereby improve the stability. Previously, Mg-vapor annealing has been applied by Wood *et al*. to improve low-temperature TE performance by reducing the grain boundary resistance via increasing the grain size.[23,39] Here we investigate the effect of Mg-vapor annealing on the thermal stability of n-type $Mg_3(Sb,Bi)_2$. We demonstrate an improved thermal stability through Mg-vapor annealing for two n-type bulk samples, $Mg_{3.5}Sc_{0.04}Sb_{1.97}Te_{0.03}$ and $Mg_3Sb_{1.475}Bi_{0.475}Te_{0.05}$. The annealing experiments were conducted using a process (Figure S1) similar to that described by Wood *et al.*[23] For $Mg_{3.5}Sc_{0.04}Sb_{1.97}Te_{0.03}$, we show that the Mg-vapor annealing does not result in a degradation of the n-type performance. The Mg-vapor annealing results in a slightly higher zT at low temperatures due to the decreased resistivity and improved power factor, but a slightly lower zT at high temperatures due to the increased thermal conductivity (Figure S6).

We found three pieces of evidence supporting the Mg migration/diffusion hypothesis. The first one is that the superior n-type properties are recovered in a degraded sample after Mg-vapor annealing, which demonstrates that elemental Mg diffuses into the grains. This is consistently observed in both this study and the report by Wood *et al.*[23] The second one is a clear increase in the Mg content in the bulk sample after Mg-vapor annealing and surface polishing revealed by SEM-EDS (see Table S3). The third piece of evidence is that elemental Mg diffuses further and in larger amounts through the bulk sample when the temperature of the Mg-vapor annealing is increased up to 635 ºC (see Figure 6a,b). For bulk samples annealed at 615 and 600 ºC (Figure 6c,d as well as Figure S7), there were only few obvious Mg particles or pieces on the surfaces, which could be removed by slightly polishing the surface. However, increasing the annealing temperature up to 635 ºC, the Mg diffusion/migration into the bulk sample significantly increased; the sample surfaces completely changed color, and there were obvious regions of elemental Mg even after a lot of polishing. The bulk $Mg_{3.5}Sc_{0.04}Sb_{1.97}Te_{0.03}$ sample after Mg-vapor annealing at 635 ºC, but prior to polishing, shows a very low resistivity of ~0.5 mΩ cm at 300 K, about nine times lower than (~4.4 mΩ cm) before Mg-vapor annealing. This is expected, as there is a significant contribution from the elemental Mg to the properties. Therefore, the Mg-vapor annealing temperature should be lower than 635 ºC to avoid making a $Mg/Mg_3(Sb,Bi)_2$ composite. Below we demonstrate the impact of Mg-vapor annealing on the thermal stability of n-type $Mg_{3.5}Sc_{0.04}Sb_{1.97}Te_{0.03}$ and $Mg_3Sb_{1.475}Bi_{0.475}Te_{0.05}$ samples. For $Mg_3Sb_{1.475}Bi_{0.475}Te_{0.05}$ the sample was Mg-vapor annealed at 600 ºC consistent with Wood *et al.*[23] for 7 days, while for $Mg_{3.5}Sc_{0.04}Sb_{1.97}Te_{0.03}$ the sample was annealed at a higher temperature of 615 ºC for a shorter time of 3 days.

The PXRD data were recorded in each step of post-treatment to keep track of the structural change after the Mg-vapor annealing and long-term stability test. The PXRD patterns in Figures 7a and 8a reveal that both $Mg_{3.5}Sc_{0.04}Sb_{1.97}Te_{0.03}$ and $Mg_3Sb_{1.475}Bi_{0.475}Te_{0.05}$ pellets maintain the main phase of Mg_3Sb_2, and show no clear structural change after the Mg-vapor annealing and long-term (L-T) Hall measurements. For $Mg_{3.5}Sc_{0.04}Sb_{1.97}Te_{0.03}$ the Mg-vapor annealing was conducted on the as-synthesized pellet after the L-T Hall measurement, while for $Mg_3Sb_{1.475}Bi_{0.475}Te_{0.05}$ the Mg-vapor annealing was conducted on the degraded sample that has become p-type after exposed to air at room temperature for a long time (≥ 1 year). After the Mg-vapor annealing, a small amount of the Mg phase was detected on the sample surface, which was easily removed after polishing the sample surface.

L-T Hall measurements were conducted at 723 K in a dynamic vacuum (< 10^{-4} mbar) in order to examine the thermal stability through the changes in the electrical resistivity, Hall carrier concentration, and mobility as functions of the measurement time (see Figures 7b-d and 8b-d).

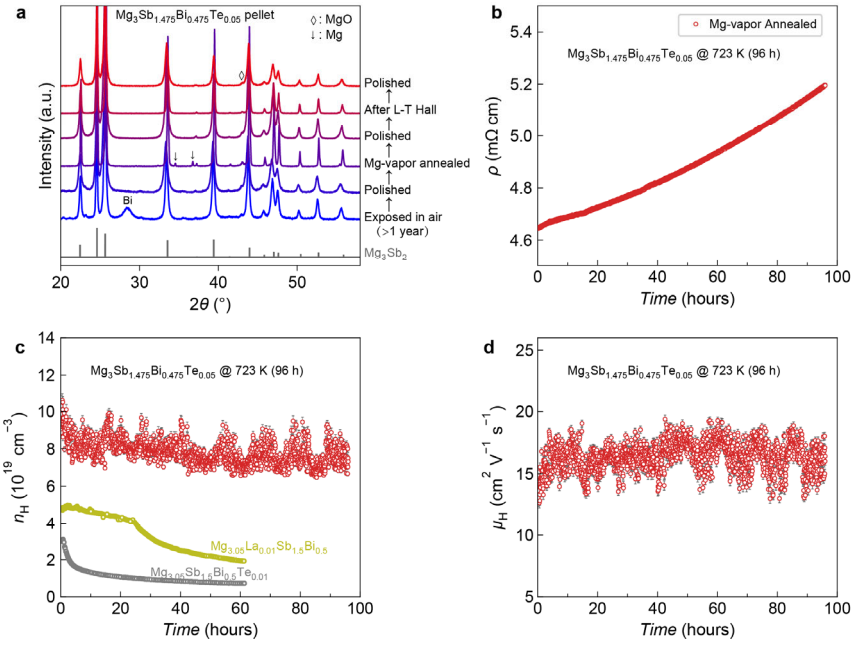

Figure 8. (a) PXRD patterns of the $Mg_3Sb_{1.475}Bi_{0.475}Te_{0.05}$ pellet after exposed in air for a long time (≥ 1 year), as well as after Mg-vapor annealing at 600 ºC for 7 days and long-term (L-T) Hall measurement. (b) Electrical resistivity, (c) Hall carrier concentration, and (d) mobility as functions of the Hall measurement time for the Mg-vapor annealed $Mg_3Sb_{1.475}Bi_{0.475}Te_{0.05}$ pellet. In (c), the data of the $Mg_{3.05}La_{0.01}Sb_{1.5}Bi_{0.5}$ and $Mg_{3.05}Sb_{1.5}Bi_{0.5}Te_{0.01}$ reported in ref. [16] are presented for comparison.

We note that the stability can be greatly enhanced when the temperature is lower than 673 K,[19] but here we chose the stability test at 723 K to accelerate the observation of property degradation. In both $Mg_{3.5}Sc_{0.04}Sb_{1.97}Te_{0.03}$ and $Mg_3Sb_{1.475}Bi_{0.475}Te_{0.05}$, we observed a significant improvement in thermal stability after the Mg vapor annealing. For $Mg_{3.5}Sc_{0.04}Sb_{1.97}Te_{0.03}$, L-T Hall measurements were performed at 723 K for 3 days (72 hours) for the same sample before and after the Mg-vapor annealing. As shown in Figure 7b, the Mg-vapor annealed $Mg_{3.5}Sc_{0.04}Sb_{1.97}Te_{0.03}$ sample exhibits a much slower increase in electrical resistivity than the as-synthesized sample for the first ~40 hours. Only after around 50 hours does the resistivity increase in the Mg-vapor annealed sample become as rapid as the immediate increase observed prior to the Mg-vapor annealing. In the context below, their absolute values are used for discussion. As illustrated in Figure 7c, when the measurement time is within 40 hours, the Hall carrier concentration of the Mg-vapor annealed sample decreases very slowly from 3.95×10^{19} to 3.30×10^{19} cm^{-3}, while the as-synthesized sample shows an exponential decay in the Hall carrier concentration from 3.25×10^{19} to 1.0×10^{19} cm^{-3}. Almost 50 hours later, the carrier concentration of the Mg-vapor annealed sample starts to decrease relatively quickly to 1.44×10^{19} cm^{-3} at the end of a total of 72 hours. Upon the Mg-vapor annealing, the carrier concentration is increased to some extent, which might be explained by the reduction of the number of electron compensating Mg vacancies. Figure 7d shows that there is no significant change in Hall mobility over the measurement time of 72 hours. According to the results and analysis above, it can be concluded that the stability of the representative n-type sample ($Mg_{3.5}Sc_{0.04}Sb_{1.97}Te_{0.03}$) is greatly enhanced through annealing at 615 ºC for 3 days in Mg-vapor.

The two distinct regions for the resistivity and carrier concentration degradations of the Mg-vapor annealed $Mg_{3.5}Sc_{0.04}Sb_{1.97}Te_{0.03}$ sample can be explained using the proposed degradation mechanism. The Mg-vapor annealing suppresses the Mg migration/loss as the grains and grain boundaries have been saturated with elemental Mg, but it does not prevent the Mg loss from the surface. As the sample surface becomes Mg-poor, the Mg will diffuse/migrate from the grain boundaries to the surface. The relatively slow degradation region is associated with the situation where the grain boundaries do not become Mg-poor and the grains do not show significant Mg loss/migration. However, when the grain boundaries become Mg-poor, significant Mg loss through the migration/diffusion from grains to grain boundaries will happen and the property degradation will turn to a rapid region as we observed in Figure 7b,c.

For the degraded sample of $Mg_3Sb_{1.475}Bi_{0.475}Te_{0.05}$ exposed in ambient conditions for more than one year, the Mg-vapor annealing was able to recover the n-type properties (Figure 8b-d). As illustrated in Figure 8b for the Mg-vapor annealed $Mg_3Sb_{1.475}Bi_{0.475}Te_{0.05}$ pellet, there is only a very small increase in the electrical resistivity from 4.65 to 5.20 mΩ cm over the entire 96 h period with an increasing rate of 5.73×10^{-3} mΩ cm h^{-1}. Figure 8c presents the time-dependent Hall carrier concentration data for the Mg-vapor annealed $Mg_3Sb_{1.475}Bi_{0.475}Te_{0.05}$ pellet in comparison with both $Mg_{3.05}La_{0.01}Sb_{1.5}Bi_{0.5}$ and $Mg_{3.05}Sb_{1.5}Bi_{0.5}Te_{0.01}$ reported in reference [14]. Obviously, the Mg-vapor annealed $Mg_3Sb_{1.475}Bi_{0.475}Te_{0.05}$ pellet shows no significant change in the carrier concentration kept at about 8×10^{19} cm^{-3} over 96 h (at 723 K). In contrast, both the reported $Mg_{3.05}La_{0.01}Sb_{1.5}Bi_{0.5}$ and $Mg_{3.05}Sb_{1.5}Bi_{0.5}Te_{0.01}$ samples[16] show a linear decrease followed by an exponential decrease in the carrier concentration within 60 h (at 723 K). In addition, the Hall mobility in the Mg-vapor annealed $Mg_3Sb_{1.475}Bi_{0.475}Te_{0.05}$ pellet is relatively stabilized at around 15 cm^2 V^{-1} s^{-1} over 96 h at 723 K (Figure 8d). Therefore, it is further confirmed that Mg-vapor annealing leads to a considerable enhancement in

the thermal stability of the n-type $Mg_3(Sb,Bi)_2$-based TE materials.

3.3.2 Other strategies

Doping with heavy elements. Doping with larger, heavier elements has been demonstrated as an effective approach for enhancing thermal stability in many well-known TE materials such as Zn_4Sb_3.[40,41] For n-type $Mg_3(Sb,Bi)_2$, doping or substituting on the Mg sites with heavier elements will greatly suppress the migration and evaporation loss of Mg from the n-type $Mg_3(Sb,Bi)_2$ grains. This method has already been confirmed to be effective with La, Yb, and Y dopants.[16-18] Other heavy lanthanide dopants are expected to show a similar improvement in thermal stability. The effect of heavy dopants is dependent on the Mg vacancy concentration as the increasing amount of Mg vacancies with time would provide void spaces and channels to facilitate the Mg migration/loss within the grains. When the concentration of Mg vacancies reaches a certain level, the degradation would return to a relatively fast speed. This is confirmed in the time-dependent Hall concentration of La-doped $Mg_3Sb_{1.5}Bi_{0.5}$ (Figure 8c).[16] Therefore, doping with heavy elements should be combined with the Mg-vapor annealing and surface coating for further improvement of the long-term thermal stability.

Surface coating. As the $Mg_3(Sb,Bi)_2$ system shows a notable surface effect, surface coating or encapsulation naturally becomes an effective strategy for improving thermal stability. The idea of surface coating is to suppress the Mg loss (through evaporation or oxidation) from the sample surface. The coating or encapsulation materials should be chemically inert, showing no reaction with the Mg and $Mg_3(Sb,Bi)_2$. Previously, BN coating has been applied and confirmed to be an effective coating material for improving the thermal stability of n-type $Mg_3(Sb,Bi)_2$.[19] In addition to BN, other coating materials such as MgO and SiC may be good options.

Mg-vapor annealing combined with surface coating. In this study Mg-vapor annealing has been confirmed to be effective in improving thermal stability; however, it does not resolve the issues of the Mg migration from grain boundaries to the surface and the Mg loss from the surface. Surface coating with MgO would help suppress the Mg loss from the sample surface. To suppress the Mg migration from grain boundaries to the surface it might be a good idea to set a migration barrier by depositing a thin layer of Mg on the surface of TE legs. Hence, we expect a combined strategy of Mg-vapor annealing and surface coating with Mg/MgO to further improve the long-term thermal stability of n-type $Mg_3(Sb,Bi)_2$ bulk materials.

4. CONCLUSIONS

Using multi-temperature X-ray and neutron scattering techniques, we have studied the thermal stability of n-type chalcogen-doped $Mg_3Sb_{1.5}Bi_{0.5}$ in both powdered and bulk forms. We show that the powdered sample exhibits a much faster degradation of being Mg-poor than the bulk sample due to a much larger exposed surface-to-volume ratio, highlighting a notable kinetic effect. The surface of the bulk sample is found to slowly become Bi-rich after being exposed to ambient conditions for a long time (longer than one year), revealing a clear surface effect and the necessity of surface encapsulation for practical applications. We then propose a detailed three-step degradation mechanism based on the Mg migration/loss for understanding the property degradation, and highlight the Mg loss of grains as the essential step for the degradation. Possible solutions for suppressing the degradation are discussed and the Mg-vapor annealing is found to be an effective, straightforward approach for improving thermal stability since it can saturate the grains and grain boundaries with the elemental Mg, which greatly suppresses the Mg migration/loss. Finally, we briefly discuss other promising strategies, and propose the combination of the Mg-vapor annealing and Mg/MgO surface coating as a potential approach for further improving the long-term thermal stability of n-type $Mg_3(Sb,Bi)_2$ for practical applications.

ASSOCIATED CONTENT

The Supporting Information is available free of charge via the Internet at http://pubs.acs.org.

Refinement results of the multi-temperature in-house powder X-ray diffraction and TOF diffraction data of $Mg_3Sb_{1.475}Bi_{0.475}Te_{0.05}$; The Mg:Sb composition ratio by SEM-EDS before and after Mg-vapor annealing; Illustration of the Mg-vapor annealing setup; Illustration of the refinements of neutron TOF diffraction data of $Mg_3Sb_{1.475}Bi_{0.475}Te_{0.05}$; Multi-temperature in-house PXRD of the powdered samples of $Mg_3Sb_{1.5}Bi_{0.48}Se_{0.02}$ and $Mg_3Sb_{1.5}Bi_{0.49}S_{0.01}$; Multi-temperature synchrotron PXRD patterns collected at the P21.1 beamline at DESY on powdered samples of $Mg_3Sb_{1.5}Bi_{0.48}Se_{0.02}$, $Mg_3Sb_{1.5}Bi_{0.49}S_{0.01}$, Mg_3Sb_2, and $Mg_3Sb_{1.5}Bi_{0.5}$; TE properties before and after Mg-vapor annealing of $Mg_{3.5}Sc_{0.04}Sb_{1.97}Te_{0.03}$; SEM-EDS Mg elemental mapping of the surface of the $Mg_3Sb_{1.475}Bi_{0.475}Te_{0.05}$ pellet annealed in Mg vapor at 600 ºC for 7 days.

AUTHOR INFORMATION

Corresponding Author

* Email: jiaweizhang@chem.au.dk; bo@chem.au.dk

Notes

The authors declare no competing financial interest.

ACKNOWLEDGMENT

We thank Karl F. F. Fischer for discussions and comments. This work was supported by the Villum Foundation and the Danish Centre for X-ray and neutron scattering (DanScatt). The synchrotron radiation experiments were performed at BL44B2 at SPring-8 in Japan under the approval of RIKEN, which is gratefully acknowledged. Kenichi Kato is acknowledged for support during synchrotron experiments at BL44B2. The authors also thank the staffs at the beamline Polaris of the ISIS Neutron and Muon Source (UK) and the PETRA III (DESY) beamline P21.1 (Swedish Materials Science Beamline) for the support.

REFERENCES

(1) Seebeck, T. J. Magnetic Polarization of Metals and Minerals by Temperature Deferences. *Abh. Preuss. Akad. Wiss.* **1822-1823**, p.265.

(2) Nolas, G. S.; Sharp, J.; Goldsmid, H. J. *Thermoelectrics: Basic Principles and New Materials Developments* (Springer, New York, 2001).

(3) Meroz, O.; Gelbstein, Y. Thermoelectric $Bi_2Te_{3-x}Se_x$ Alloys for Efficient Thermal to Electrical Energy Conversion, *Phys. Chem. Chem. Phys.* **2018**, *20*, 4092-4099.

(4) Pedersen, S. H. *Thermoelectric Properties of Zintl Compounds* $Mg_3Sb_{2-x}Bi_x$ (Chemistry Project for Master's Degree, Department of Chemistry, Aarhus University, 2012). See http://chem.au.dk/fileadmin/cmc.chem.au.dk/pictures_new_homepage

/Pedersen_S_H_-_Thermoelectric_Properties_of_Zintl_Compounds_Mg3Sb2-xBix.pdf.

(5) Zhang, J.; Song, L.; Pedersen, S. H.; Yin, H.; Hung, L. T.; Iversen, B. B. Discovery of High-Performance Low-Cost N-Type Mg_3Sb_2-Based Thermoelectric Materials with Multi-Valley Conduction Bands. *Nat. Commun.* **2017**, *8*, 13901.

(6) Tamaki, H.; Sato, H. K.; Kanno, T. Isotropic Conduction Network and Defect Chemistry in $Mg_{3+\delta}Sb_2$-Based Layered Zintl Compounds with High Thermoelectric Performance. *Adv. Mater.* **2016**, *28*, 10182-10187.

(7) Shuai, J.; Mao, J.; Song, S.; Zhu, Q.; Sun, J.; Wang, Y.; He, R.; Zhou, J.; Chen, G.; Singh, D. J.; Ren, Z. Tuning the Carrier Scattering Mechanism to Effectively Improve the Thermoelectric Properties. *Energy Environ. Sci.* **2017**, *10*, 799-807.

(8) Imasato, K.; Kang, S. D.; Snyder, G. J. Exceptional Thermoelectric Performance in $Mg_3Sb_{0.6}Bi_{1.4}$ for Low-Grade Waste Heat Recovery. *Energy Environ. Sci.* **2019**, *12*, 965-971.

(9) Mao, J.; Zhu, H.; Ding, Z.; Liu, Z.; Gamage, G. A.; Chen, G.; Ren, Z. High Thermoelectric Cooling Performance of N-Type Mg_3Bi_2-Based Materials. *Science* **2019**, *365*, 495-498.

(10) Pan, Y.; Yao, M.; Hong, X.; Zhu, Y.; Fan, F.; Imasato, K.; He, Y.; Hess, C.; Fink, J.; Yang, J.; Büchner, B.; Fu, C.; Snyder, G. J.; Felser, C. $Mg_3(Bi,Sb)_2$ Single Crystals Towards High Thermoelectric Performance. *Energy Environ. Sci.* **2020**, *13*, 1717-1724.

(11) Shu, R.; Zhou, Y.; Wang, Q.; Han, Z.; Zhu, Y.; Liu, Y.; Chen, Y.; Gu, M.; Xu, W.; Wang, Y.; Zhang, W.; Huang, L.; Liu, W. $Mg_{3+\delta}Sb_xBi_{2-x}$ Family: A Promising Substitute for the State-of-the-Art N-Type Thermoelectric Materials Near Room Temperature. *Adv. Funct. Mater.* **2019**, *29*, 1807235.

(12) Liu, Z.; Sato, N.; Gao, W.; Yubuta, K.; Kawamoto, N.; Mitome, M.; Kurashima, K.; Owada, Y.; Nagase, K.; Lee, C.-H.; Yi, J.; Tsuchiya, K.; Mori, T. Demonstration of Ultrahigh Thermoelectric Efficiency of ~7.3% in Mg_3Sb_2/MgAgSb Module for Low-Temperature Energy Harvesting. *Joule* **2021**, *5*, 1196-1208.

(13) Yang, J.; Li, G.; Zhu, H.; Chen, N.; Lu, T.; Gao, J.; Guo, L.; Xiang, J.; Sun, P.; Yao, Y.; Yang, R.; Zhao, H. Next-Generation Thermoelectric Cooling Modules Based on High-Performance $Mg_3(Bi,Sb)_2$ Material. *Joule* **2022**, *6*, 193-204.

(14) Liang, J.; Yang, H.; Liu, C.; Miao, L.; Chen, J.; Zhu, S.; Xie, Z.; Xu, W.; Wang, X.; Wang, J.; Peng, B.; Koumoto, K. Realizing a High ZT of 1.6 in N-Type Mg_3Sb_2-Based Zintl Compounds through Mn and Se Codoping. *ACS Appl. Mater. Interfaces* **2020**, *12*, 21799-21807.

(15) Jørgensen, L. R.; Zhang, J.; Zeuthen, C. B.; Iversen, B. B. Thermal Stability of $Mg_3Sb_{1.475}Bi_{0.475}Te_{0.05}$ High Performance N-Type Thermoelectric Investigated through Powder X-ray Diffraction and Pair Distribution Function Analysis. *J. Mater. Chem. A* **2018**, *6*, 17171-17176.

(16) Imasato, K.; Wood, M.; Kuo, J. J.; Snyder, G. J. Improved Stability and High Thermoelectric Performance through Cation Site Doping in N-Type La-Doped $Mg_3Sb_{1.5}Bi_{0.5}$. *J. Mater. Chem. A* **2018**, *6*, 19941-19946.

(17) Shi, X.; Zhao, T.; Zhang, X.; Sun, C.; Chen, Z.; Lin, S.; Li, W.; Gu, H.; Pei, Y. Extraordinary N-Type Mg_3SbBi Thermoelectrics Enabled by Yttrium Doping. *Adv. Mater.* **2019**, *31*, 1903387.

(18) Wood, M.; Imasato, K.; Anand, S.; Yang, J.; Snyder, G. J. The Importance of the Mg–Mg Interaction in Mg_3Sb_2–Mg_3Bi_2 Shown through Cation Site Alloying. *J. Mater. Chem. A* **2020**, *8*, 2033-2038.

(19) Shang, H.; Liang, Z.; Xu, C.; Song, S.; Huang, D.; Gu, H.; Mao, J.; Ren, Z.; Ding, F. N-type $Mg_3Sb_{2-x}Bi_x$ with Improved Thermal Stability for Thermoelectric Power Generation. *Acta Mater.* **2020**, *201*, 572-579.

(20) Zhang, J.; Song, L.; Mamakhel, A.; Jørgensen, M. R. V.; Iversen, B. B. High-Performance Low-Cost N-Type Se-Doped Mg_3Sb_2-Based Zintl Compounds for Thermoelectric Application. *Chem. Mater.* **2017**, *29*, 5371-5383.

(21) Zhang, J.; Song, L.; Borup, K. A.; Jørgensen, M. R. V.; Iversen, B. B. New Insight on Tuning Electrical Transport Properties via Chalcogen Doping in N-Type Mg_3Sb_2-Based Thermoelectric Materials. *Adv. Energy Mater.* **2018**, *8*, 1702776.

(22) Zhang, J.; Song, L.; Iversen, B. B. Rapid One-Step Synthesis and Compaction of High-Performance N-Type Mg_3Sb_2 Thermoelectrics. *Angew. Chem. Int. Ed.* **2020**, *59*, 4278-4282.

(23) Wood, M.; Kuo, J. J.; Imasato, K.; Snyder, G. J. Improvement of Low-Temperature zT in a Mg_3Sb_2–Mg_3Bi_2 Solid Solution via Mg-Vapor Annealing. *Adv. Mater.* **2019**, *31*, 1902337.

(24) Kato, K.; Hirose, R.; Takemoto, M.; Ha, S.; Kim, J.; Higuchi, M.; Matsuda, R.; Kitagawa, S.; Takata, M. The RIKEN Materials Science Beamline at SPring-8: Towards Visualization of Electrostatic Interaction. *AIP Conf. Proc.* **2010**, *1234*, 875-878.

(25) Hull, S.; Smith, R. I.; David, W. I. F.; Hannon, A. C.; Mayers, J.; Cywinski, R. The Polaris Powder Diffractometer at ISIS. *Physica B* **1992**, *180-181*, 1000-1002.

(26) Rodríguez-Carvajal, J. Recent Advances in Magnetic Structure Determination by Neutron Powder Diffraction. *Physica B* **1993**, *192*, 55-69.

(27) Thompson, P.; Cox, D. E.; Hastings, J. B. Rietveld Refinement of Debye-Scherrer Synchrotron X-ray Data from Al_2O_3. *J. Appl. Crystallogr.* **1987**, *20*, 79-83.

(28) Petricek, V.; Dusek, M.; Palatinus, L. Crystallographic Computing System JANA2006: General Features. *Z. Kristallogr.* **2014**, *229*, 345.

(29) Pauw, L. J. v. d. A Method of Measuring Specific Resistivity and Hall Effect of Discs of Arbitrary Shape. *Philips Res. Rep.* **1958**, *13*, 1-9.

(30) Borup, K. A.; Toberer, E. S.; Zoltan, L. D.; Nakatsukasa, G.; Errico, M.; Fleurial, J.-P.; Iversen, B. B.; Snyder, G. J. Measurement of the Electrical Resistivity and Hall Coefficient at High Temperatures. *Rev. Sci. Instrum.* **2012**, *83*, 123902.

(31) Iwanaga, S.; Toberer, E. S.; LaLonde, A.; Snyder, G. J. A High Temperature Apparatus for Measurement of the Seebeck Coefficient. *Rev. Sci. Instrum.* **2011**, *82*, 063905.

(32) Song, L.; Zhang, J.; Iversen, B. B. Thermal Stability of P-Type Ag-Doped Mg_3Sb_2 Thermoelectric Materials Investigated by Powder X-Ray Diffraction. *Phys. Chem. Chem. Phys.* **2019**, *21*, 4295-4305.

(33) Ohno, S.; Imasato, K.; Anand, S.; Tamaki, H.; Kang, S. D.; Gorai, P.; Sato, H. K.; Toberer, E. S.; Kanno, T.; Snyder, G. J. Phase Boundary Mapping to Obtain N-Type Mg_3Sb_2-Based Thermoelectrics. *Joule* **2018**, *2*, 141-154.

(34) Gorai, P.; Ortiz, B. R.; Toberer, E. S.; Stevanovic, V. Investigation of N-Type Doping Strategies for Mg_3Sb_2. *J. Mater. Chem. A* **2018**, *6*, 13806-13815.

(35) Peng, W.; Petretto, G.; Rignanese, G. M.; Hautier, G.; Zevalkink, A. An Unlikely Route to Low Lattice Thermal Conductivity: Small Atoms in A Simple Layered Structure. *Joule* **2018**, *2*, 1879-1893.

(36) Zhang, J.; Song, L.; Sist, M.; Tolborg, K.; Iversen, B. B. Chemical Bonding Origin of the Unexpected Isotropic Physical Properties in Thermoelectric Mg_3Sb_2 and Related Materials. *Nat. Commun.* **2018**, *9*, 4716.

(37) Zhang, J.; Song, L.; Iversen, B. B. Insights into the Design of Thermoelectric Mg_3Sb_2 and Its Analogs by Combining Theory and Experiment. *npj Comput. Mater.* **2019**, *5*, 76.

(38) Kuo, J. J.; Yu, Y.; Kang, S. D.; Cojocaru-Mirédin, O.; Wuttig, M.; Snyder, G. J. Mg Deficiency in Grain Boundaries of N-Type Mg_3Sb_2 Identified by Atom Probe Tomography. *Adv. Mater. Interfaces* **2019**, *6*, 1900429.

(39) Kuo, J. J.; Kang, S. D.; Imasato, K.; Tamaki, H.; Ohno, S.; Kanno, T.; Snyder, G. J. Grain Boundary Dominated Charge Transport in Mg_3Sb_2-Based Compounds. *Energy Environ. Sci.* **2018**, *11*, 429-434.

(40) Pedersen, B. L.; Yin, H.; Birkedal, H.; Nygren, M.; Iversen, B. B. Cd Substitution in $M_xZn_{4-x}Sb_3$: Effect on Thermal Stability, Crystal Structure, Phase Transitions, and Thermoelectric Performance. *Chem. Mater.* **2010**, *22*, 2375-2383.

(41) Song, L.; Blichfeld, A. B.; Zhang, J.; Kasai, H.; Iversen, B. B. Enhanced Thermoelectric Performance and High-Temperature Thermal Stability of P-Type Ag-Doped β-Zn_4Sb_3. *J. Mater. Chem. A* **2018**, *6*, 4079-4087.

Table of Content:

Enhanced thermal stability through suppressing the Mg loss/migration